Damage evolution of hot-pressed boron carbide under confined dynamic compression

L. Farbaniec[a,1,*], J. D. Hogan[a,b], K. Y. Xie[c], M. Shaeffer[a], K. J. Hemker[c], K. T. Ramesh[a,c]

[a] *Hopkins Extreme Materials Institute, The Johns Hopkins University, Baltimore, MD 21218, USA*
[b] *Department of Mechanical Engineering, University of Alberta, Edmonton, AB T6G 2R3, Canada*
[c] *Department of Mechanical Engineering, The Johns Hopkins University, Baltimore, MD 21218, USA*

Abstract

The dynamic response of hot-pressed boron carbide was studied under uniaxial and confined loading conditions using a modified compression Kolsky bar setup at strain rates of 10^2 – 10^3 s^{-1}. The progression of damage in the prismatic specimens was captured using a high-speed camera. This experimental approach was reproduced in a quasi-static regime (10^{-4} – 10^{-3} s^{-1}) to study the rate dependance of the strengths and damage modes. The results showed that the compressive strength of boron carbide was both stress state and strain rate dependent. A real-time visualization showed a change in the crack path under confined compression loading. Our observations revealed the formation of column-like fragments and slabs in the uniaxial and confined compression, respectively. Collected fragments of the specimens were used to investigate failure mechanisms by SEM and TEM. Both observations showed transgranular fracture. It was found that microcracks originate at large carbon inclusions and have tensile character. TEM examinations also point to the absence of stress-induced damage at grain boundaries and inside boron carbide grains. The formation of microcracks was responsible for experimentally observed inelastic response un-

*Corresponding author: Lukasz Farbaniec (lfarban1@jhu.edu)
[1] Present address: Institute of Shock Physics, Imperial College London, London SW7 2AZ, UK

der dynamic loading conditions.

Keywords: Boron carbide, Kolsky bar technique, Confined compression, Brittle failure

1. Introduction

Ceramics are the material of choice for many structural applications because of superior hardness and strength-to-weight ratio. In practice, their resistance to failure is often measured based on uniaxial compression experiments, even though in most applications true uniaxial conditions are not common. For example, ceramics used as protective layers in high-velocity impact applications experience multi-axial stress states during the impact. Boron carbide (BC) is one such ceramic that has recently gained much interest in this field of research because of its applications in personnel protection [1, 2, 3, 4, 5]. These require a significant amount of effort to evaluate the dynamic failure strength of BC in shock wave experiments (see, for example, [6, 7, 8, 9, 10, 11]). Like most ceramics, BC is strong in compression, but its performance is poor in tensile or multi-axial stress conditions. There appears to be no appreciable plasticity in BC materials [12]. Substantial efforts are therefore made to improve the overall performance of advanced ceramics, like BC.

An effective way to enhance the mechanical response of brittle materials is by tailoring their microstructure, for example by introducing ductile interfaces or grain-boundary films [13, 14, 15, 16]. Many studies [17, 18, 19, 20, 21, 22, 23, 24] have also examined the effects of confinement on the mechanical behavior of ceramics as a way to increase their performance. The application of additional pressure effectively suppresses unstable growth of tension cracks and delays catastrophic failure. In terms of high loading rates, confined dynamic compression tests on ceramics have been performed under triaxial stress states [17, 18]. These experiments were conducted on cylindrical specimens with a shrink-fit metal sleeve that generated a uniformly distributed hydrostatic pressure on the lateral surface. In [18], for example, a remarkable increase in the fracture

strength of AlN (from 2.5 GPa to 4.0 GPa) was observed by applying a confinement pressure of approximately 230 MPa. Such studies provide more valuable insights in terms of the resulting strength rather than the damage development because of loss of cylindrical symmetry and difficulty of visualization.

The effect of confinement on the dynamic mechanical response of structural ceramics under biaxial compression was examined by Ramesh and co-workers [19, 20]. These experiments were conducted by applying loads (one static and one dynamic) in two principal directions of the prismatic sample, while visualizing the free surface in the third direction. The intention of these studies was to visualize the crack propagation behavior on the free surface under a sufficiently large static pressure. It was demonstrated by [19] that by applying the static confinement pressure of approximately 400 MPa, the dynamic strength of AlON increases from 3.45 GPa to 4.05 GPa. This confined compression technique provides valuable insights into the understanding of failure mechanisms and damage development through a real-time visualization of the cracking process but is not able to provide full confinement.

The mechanisms underlying microcrack formation in brittle solids have been studied for many years, and are well understood [25, 26, 27, 28, 29]. In the crack nucleation process, the intrinsic microstructural inhomogeneities (e.g. inclusions, pores and grain-boundary films) are crucial contributors influencing the structural stability of the material and lead to the formation of cracks under certain critical loading conditions. Once these cracks are nucleated, the propagation direction depends on the stress field in front of the crack tip. In a typical scenario, this stress field is strongly affected by surrounding inhomogeneities and cracks. This complex system of dynamically interacting cracks remains one of the most fundamental theoretical problems in the mechanics of brittle solids. Experimental methods for studying material response at different stress state, such as discussed herein, can help address this issue.

2. Experimental procedure

A detailed characterization of this BC microstructure is provided in our previous studies [30, 31, 32, 33]. Prismatic specimens with dimensions of 3.5 mm ×4 mm ×5.3 mm (and subsequently attached coordinate system: X1, X2 and X3), were cut from a plate 8 mm thick. The coordinate system is associated with the plate in the following manner: X1 and X2 are principal directions lying in the hot-pressed surface; X3 is the hot-pressing (and the largest compressive principal loading) direction. In the case of confined compression experiments, a static confinement was applied in the X2 direction. A prismatic specimen geometry was chosen for testing for a few reasons. First, the macroscopic failure path in one principal specimen dimension can be visualized using a high-speed camera. Second, the confinement effect on the failure behavior can be studied using the same specimen geometry as used in uniaxial compression. The advantage of biaxial confinement over sleeve or hydraulic confinement is that the stress state in the specimen is better known [17, 19]. Consequently, a confined compression experiment allows us to visualize the change in the failure path on the free surface, and to verify if the scatter of the results comes from microstructure variability.

The schematic of a Kolsky bar technique for high-strain-rate compression experiments is presented in Fig. 1. This is an established technique, but some crucial experimental details are provided here (these are important for testing ceramics). Bars and projectile were made of ultra-high-strength maraging steel having a diameter of 12.7 mm. In order to adopt the experimental approach for dynamic testing of brittle materials, the following improvements have been made. First, a pulse-shaping technique using thin sheets of copper and graphite between incident bar and projectile was adopted. This ensures relatively constant loading rate and stress equilibrium in the specimen before failure. Second, impedance-matched tungsten carbide (WC) disks confined by a heat-shrunk Ti-6Al-4V collar were used between the Kolsky bars and the specimen. This prevents the damage of bars due to indentation from the sample. In order to

reduce the interfacial friction between the specimen ends and WC disks, lubrication was provided at this interface. Finally, we note that the specimen strain measurement in the case of very hard ceramic materials is dubious. In this study, the strain rate was estimated based on the stress-time history.

The confined dynamic compression experiment (configuration B) was carried out as follows. First, the specimen was sandwiched between two high-strength steel T-blocks. Next, four screws were tightened with controlled equal torques, what generated a quasi-static compressive stress of about 500 MPa along the X2 direction. To reduce stress concentration between the specimen and T-blocks, AISI 4140 low-alloy steel 'cushions' of 0.5 mm thickness were used. A more detailed description of the assembly and experimental procedure is provided in Ref. [19]. The failure process was captured by a high-speed camera (capable of capturing images at up to 2 million frames per second) and correlated with the stress-time curve. In both experimental configurations, the sample domain was covered with a polycarbonate box to collect the fragments for further analysis.

The quasi-static mechanical behavior was investigated using a standard MTS machine at strain rates of 10^{-4} – 10^{-3} s^{-1} and room temperature. Similarly to the dynamic case, WC plates were used to protect the compression platens from the potential indentation coming from the sample. A high-speed camera with a speed of 256 thousand frames per second was used to visualize the failure process. In this case, however, the camera was manually triggered and failure process was not correlated with stress-time history. The assembly for confined quasi-static compression experiments (Fig. 2) is composed of the same components as the confined dynamic compression experimental design. Because of the reorientation of the principal loading, additional supporting blocks were used to ensure the alignment with compression platens and to accurately transmit the compression load through bars between the specimen and compression platens.

Fragments of the specimens for all experimental configurations were collected and investigated using electron microscopy. A TESCAN MIRA3 field emission Scanning Electron Microscope (SEM) was used to identify failure mechanisms at the micrometer scale and larger, whereas CM300 Transmission Electron Mi-

croscope (TEM) was used to study fragments at the sub-micrometer scale and smaller. Two types of TEM investigations on fragments were performed. In the first case, the smallest fragments up to a few hundred nanometers in size were freely suspended on a holey carbon grid, and electron transparent edges were searched for the evidence of inelastic deformation and damage. In the second case, the larger fragments were prepared by mechanical polishing on a series of diamond lapping papers (30µm–100nm) using a tripod polisher to create a thin wedge. The specimens were further thinned to electron transparency with ion milling at 4kV and 1mA.

3. Experimental results

3.1. High-speed image observations

The stress-time histories for typical dynamic compression experiments and the corresponding high-speed camera images are shown in Figs. 3(a–c). In both cases, the stresses inside the specimen initially build up without perceptible fracturing on the free surface (Photographs 1–2 in Fig. 3b and Photograph 1 in Fig. 3c). The first cracks at the edges of the specimen are visible ∼3 µs before the peak stresses (indicated by the white arrows in Photograph 3 in Fig. 3b and Photograph 2 in Fig. 3c). The change in the stress-time slope between the first visible cracks and the moment of peak stress is noticeable. Such change in material response, however, is not surprising and has been also observed in the case of other advanced ceramics [19, 20, 34]. Note that there is no direct evidence in the literature to support the hypothesis that commercial hot-pressed boron carbide ceramics deforms plastically through dislocation activity, twinning or other microstructure-related mechanisms in the investigated regimes of stress, strain rate and temperature. Therefore, this behavior is most likely related to the microcracks development from pre-existing microstructural inhomogeneities, as reported in Ref. [31]. Such development and propagation of microcracks eventually lead to stress relaxation without the occurrence of

plastic deformation. After the peak stress, a catastrophic stress drop occurs, accompanied by large scale cracking and ultimate failure.

Note that the stresses built up in the specimens with different rates of time. The average stress rate under uniaxial and confined dynamic compression tests was 174 MPa/µs and 360 MPa/µs, respectively. Consequently, the strain rate values estimated based on the stress-time history were higher in confined dynamic compression tests. Since all Kolsky bar experiments were conducted using the same experimental procedure, the cause of the stress rate sensitivity is unclear. However, it is speculated that the confinement (which is applied to the specimen before the test) affects the reflections of the stress waves from the surfaces of the specimen, which are in contact with the T-blocks (see Fig. 1). Consequently, the damage part of the related strain rate component in the confined direction (associated with the buckling rate of the damage material) is also different from that of uniaxial compression. In other words, the cracks that developed under high stress states separate the material into subregions. At this stage, the material is still intact and has to be isolated to experience the unloading state. The applied confinement limits the process of opening of the cracks, and what follows, reduces the volume of internal voids in the material. This additional constraint keeps the material as a 'solid-like', provides favorable conditions for interacting waves, and consequently stresses builds up faster in the specimen. These also results in a higher peak stress as the stress builds up with time.

The high-speed images also show a change in the failure mode between uniaxial and confined loading conditions. In the case of dynamic uniaxial compression (the compression axis is indicated by the blue arrow), cracks visible on the free surface propagate approximately parallel to the dynamic compression axis, and then are accompanied by series of perpendicular cracks contributing to further fragmentation of the specimen (Photographs 3–6 in Fig. 3b). Note that the propagation of the cracks is the same for all free surfaces, which results in formation of column-like fragments. Since the amount energy released during these processes is high, the fragments are forced to expand, and subjected to

buckling. These lead to further fragmentation. In confinement experiments, the axial splitting failure mode is no longer observed. Instead, new cracks develop in two directions (toward the main compression axis and confinement axis) almost simultaneously, inducing a mixed mode of cracking (Photographs 3–6 in Fig. 3c). The main compression axis and confinement axis are indicated by the blue and green arrows, respectively. More detailed discussion about the failure mode based on fractographic observations is provided in the later part of the manuscript.

For comparison the high-speed images from a confined quasi-static compression test are shown in Fig. 4. The high-speed imaging technique here was only used to capture the failure mode, and the integrated stress-time series with corresponding images are not provided. As in the previous case, the main compression axis is indicated by the blue arrow and the confinement axis is indicated by the green arrows. This sequence of images shows a similar failure mechanism as in the confined dynamic compression tests (Fig. 3c). The multiaxial crack path that developed on the free surface is analogous to the previously discussed results. However, based on general observations, it seems that the density of cracks developed under quasi-static conditions is lower in comparison to the dynamic case. This is also reflected in larger fragment sizes, as reported by Hogan *et al.* [30]. Similar observations to the confined quasi-static compression were made on specimens experienced quasi-static uniaxial loading conditions. In this case, the axial splitting and larger fragment size (as compared to analogous dynamic case) were observed.

3.2. Strength response

Figure 5 shows the measured peak stress values ('strengths') for the strain rates and stress states investigated. Note the trend (although not statistically significant) for increasing compressive strength at higher loading rates. Similar strain rate dependence of peak stress was reported for other boron carbides and advance ceramics in the past [19, 35, 36]. This behavior can be interpreted in terms of a mode–I crack growth controlled by different mechanisms in these two

strain rate regimes. For example, in quasi-static regime, the strength of materials is mostly controlled by the nucleation and growth of microcracks from large processing-induced defects. The process of nucleation and dramatic growth of these microcracks originates from localized tensile fields around inhomogeneities, as was demonstrated for ceramics like Al_20_3, Si_3N_4, and SiC [37, 38]. It is assumed that such a mechanism dominates up to the strain rate of $\sim 10^2$ s^{-1}. In dynamic regime, the observed increase in strength is related to the concept of crack inertia as a factor controlling failure of the materials [36].

Another observation is that higher strengths are developed in the confined specimens (most clear in the dynamic regime). This increase in strength is most likely related to the fact that the confinement suppresses the development of microcracks. This is due to a lower stress intensity factor at the crack tip, which effectively delays the onset of microcracking and results in increased peak strengths [39, 40, 36]. Note that the scatter of the results in dynamic regime is very similar for uniaxial and confined case. It indicates that this scatter is related to the variation in the microstructure, and not errors in experimental technique.

We note that several of our quasi-static experiments were unsuccessful. This is because the compression test of small size specimens by using the MTS universal machine has certain restrictions. For example, the specimen needs to be nearly perfectly positioned between compression platen of the machine to ensure uniform loading across the top surfaces of the specimen. If these conditions are not met, the stress concentration appears at the edges of the specimen when a higher force is applied. Consequently, this leads to premature failure of the specimen through early 'chipping' during load. In several cases we noted that the specimen chipped off during the test and failed at relatively low applied stress levels. We do not believe that these pre-fractured results are useful, but are included in Fig. 5.

3.3. Fractography

Fracture surface observations of collected fragments provide further insight into failure mechanisms. Figure 6(a) shows a flake-like free carbon inclusion (labelled 'C') which developed cracks from the upper and lower part of its contours in the direction of the compression axis. Here, the compression axis runs approximately vertically in the figure (indicated by the blue arrow). Note that the compressive stress direction is only approximate, and is based on the evaluation of the resulting fracture surface and the orientation of the large flake-like free carbon inclusion. For more details on the orientation of these large carbon inclusions in a hot-pressed BC plate the reader is referred to Ref. [31]. The geometry of the inclusion and crack propagation direction suggest the so-called wing crack mechanism [39, 41, 42, 31]. Figure 6b shows the edge of a fragment populated with carbon inclusions (labelled 'C'). As indicated (by the white arrows), the cracks initiated from these inclusions were able to grow extensively, forming relatively flat fracture surfaces from inclusion to inclusion, and contribute to the fragmentation process. The orientation of inclusions with respect to the compressive load (approximately indicated by the blue arrow) suggests that these cracks contributed to the axial splitting observed in high-speed images (Fig. 3b).

These examples show that the dominant failure mechanism is transgranular. Once the crack initiates from an inclusion, the propagation direction is in general consistent with the main compression axis. The crack can be deflected through other inclusions in front of the crack tip, but does not appear to be deflected when crossing the grains. Such an example is shown in Fig. 7a, with one boxed area of interest shown at higher magnification in Fig 7b. In the figure, the crack propagates from inclusion to inclusion (labelled as 'C') with little or no deflection when traversing the grain boundaries (labelled as 'GB'). These mechanisms were observed in all studied specimens.

The failure modes were different for uniaxial and confined compression. For example, if the specimen is subjected to uniaxial compression, a few cracks can propagate and interact to give a failure on planes parallel to the dominant stress

component (as shown in Figs. 6–7). However, an additional confining stress can prevent this unstable crack growth and change the failure mode. Figures 8(a–b) show the specimens after confined quasi-static compression, where exposed are the free surface of the sample (Fig. 8a) and the surface that was in contact with the WC disk, and which experienced the major compressive load (Fig. 8b). The main compression axis and confinement axis are indicated by the blue and green arrows, respectively. It should be noted that in such experiments the MTS machine was stopped at the moment of load drop to prevent any further damage. In this case, as two compression forces act in two directions, only the third principal axis (free surface used for visualization) is available for expansion. Since it is the only stable direction for the crack growth, these cracks propagate catastrophically parallel to the plane of the free surface, and split into slabs that contain both loading axes.

A few cracks can also be observed in the direction perpendicular to applied loads (indicated by the white arrows in Fig. 8b). These cracks, however, are mostly within single slabs, and do not go through the whole specimen dimension. This suggests that they were formed at the later stages of deformation. Figure 8a shows the fracture surface of the specimen in the X1 direction (free surface). Note that this fracture surface is nearly flat through the entire specimen, suggesting that the crack was initiated from a single or a few inclusions interacting in the same failure plane. The upper side of the specimen shows characteristic buckling behavior (the last stage of failure), where the material is separated in the perpendicular direction to the principal compressive load (Fig. 8b). We hypothesize that the similar failure modes are present under dynamic loading conditions. However, it is challenging to visualize these phenomena because of the dynamic character and the difficulty of stopping structural failure in the dynamic experiment.

3.4. TEM investigation

Figure 9 shows the bright-field TEM micrographs of the fragments of the specimen subjected to confined dynamic compression. These fragments are of

particular interest because the confined dynamic compression experiment result in the highest stress state at failure. Systematic tilting experiments of more than 20 fragments showed no stress-induced dislocations or deformation twins. This suggests a lack of inelastic deformation or internal damage. It is also interesting to note that many fragments contain grain boundaries. One typical example is shown in Fig. 9a, which is composed of at least three grains (triple junction indicated by the arrow) with clearly visible grain boundaries. These grain boundaries are sharp with no indication of cavitation damage. Note that the edges of many fragments are very sharp and smooth. This observation agrees well with those made by SEM (Fig. 6b) and confirms that the grain boundaries are very strong and promote transgranular fracture. Figure 9b provides more insight into the crack propagation mechanisms. The exposed fracture surface of the fragment is more rough, and populated by cleavage steps (indicated by the arrows). These fracture features most likely appeared as a consequence of the crack propagation through neighboring grains with highly twisted boundaries [43]. The SEM investigations revealed that these fracture features are very common (such steps and ridges on the fracture surface can be observed in Fig. 6b). In this regard, Fig. 9a shows the fragment with a very smooth surface, indicating a possible crack propagation through tilted grains [43]. Figure 9c shows the internal microstructure of a large fragment that contains multiple grains (note that this fragment was polished down and further thinned to electron transparency). The microstructure was free from damage and cracks. There was no apparent change in the fraction of observed defects, such as dislocation, stacking fault and twin density resulting from the impact events. For comparison, the TEM micrograph of the intact material is presented in Fig 9d. Note in the central part of the figure the flake-like free carbon inclusion (labelled as 'C').

3.5. Suppression of wing crack formation

The presented results have shown that the strength of this BC is flaw-controlled for the investigated strain rates. That is to say, the strength of the material results from the interacting wing cracks, which developed from the

intrinsic microstructural inhomogeneities. This was also true in the case of the confined dynamic compression. It means that a higher confining pressure is needed in order to shut down present failure mechanisms and activate potentially new mechanisms. The driving force for the nucleation of the crack is the critical stress intensity factor for mode–I, K_{IC}. The wing crack mechanism is not likely to be developed in the case of the K_{IC} value close to zero [20, 39, 41] (this applies to the confined compression). In this regard, the mode–I stress intensity factor (K_I) at the tips of the wing crack can be expressed as

$$K_I = \sqrt{\frac{\pi a}{3}} \left\{ (\sigma_2 - \sigma_1)\sqrt{1+\mu^2} + \mu(\sigma_2 + \sigma_1) \right\} = 0 \tag{1}$$

where, σ_1 in the applied compressive stress, σ_2 in the applied confining stress, $2a$ is the preexisting flaw size, and μ is the coefficient of friction.

Thus, based on the theoretical considerations outlined above, the wing crack mechanism can be suppressed if σ_1 is balanced by σ_2 as follow

$$\sigma_2 = c\sigma_1 \tag{2}$$

where

$$c = \frac{(1+\mu^2)^{\frac{1}{2}} - \mu}{(1+\mu^2)^{\frac{1}{2}} + \mu} \tag{3}$$

Assuming plane strain conditions, one can compute σ_2, and what follows, the 'shut down' pressure [20] for a given σ_1 as

$$p = \frac{2(1+v)(1+\mu^2)^{\frac{1}{2}}}{3(1+\mu^2)^{\frac{1}{2}} + \mu}\sigma_1 \tag{4}$$

where v is the Poisson's ratio.

If one assumes, for the sake of discussion, that $v = 0.17$, $\mu = 0.15$ [44], and applied $\sigma_1 = -3.75$ GPa (that is close to the average dynamic uniaxial compression of this BC), the 'shut down' pressure calculated from Eq. (4) is of the order of –2.5 GPa. This pressure value is significantly higher than those pressure levels imposed during the confined dynamic compression tests presented here. In our experimental setup, the confinement effectively reduced the mode–I stress intensity factor and delayed the microcracking mechanisms

to higher levels of the most compressive principal stress. However, these were not high enough to activate new failure mechanisms.

It is generally recognized that such microcracks constitute the dominant fracture mechanism in BC materials over wide range of the stress states and strain rates. It was demonstrated for many ceramics that a high compressive state, such as generated in the so-called Mescall zone under sphere-impact experiments, can activate severe microcraking (and damage) [45, 46]. This highly damage zone was not observed in the case of BC with impact velocities up to ∼300 m/s [45]. However, Chen et al. [3] observed shock induced local amorphization in BC fragments impacted at higher velocities (∼900 m/s). This suggests that localized shock amorphization is a potential high-rate mode of deformation. Nevertheless, the results of this study showed that the material responds elastically, and there is no evidence for additional mechanisms, at least for this material and investigated strain rates and stress states.

3.6. Evolution of failure mechanisms

Finally, a link between material response, failure visualization and fractography can be established. Figure 9 shows schematics of initialization and evolution of failure for investigated specimen geometry and loading conditions. When the specimen experiences uniaxial loading conditions, stress concentrations first develop in the vicinity of large carbon inclusions. The orientation of these inclusions plays an important role in the failure initiation, as discussed in [31]. Note that a single inhomogeneity can lead to the catastrophic failure of the structure in the quasi-static case. This can explain the lower compressive strength as compared to the dynamic case, in which stresses are distributed as a results of activation of a larger number of inhomogeneities. Once these flaws activate cracks, the propagation direction is aligned parallel to the direction of maximum compression. Further unstable crack growth leads to structure separation forming column-like fragments. These columns expand in the direction normal to free surfaces due to the large amount of released energy. At this stage, buckling occurs leading to further fragmentation.

A confined compression leads to changes in the macroscopic failure response. As in the uniaxial case, the specimen experiences stress concentrations in the vicinity of carbon inclusions, but the resulting crack tip driving forces are smaller and give rise to higher damage tolerance of the specimen (as discussed in Section 3.2). Note that the nucleated cracks are constrained in two directions. This leads to preferential propagation of these cracks in both loading directions, and further slab development. Similar to the uniaxial case, the slabs are then subjected to buckling due to the expansion in the third principal axis (normal to the free surface). This leads to a mixed mode of cracking, as revealed by the high-speed camera images.

4. Summary

A modified Kolsky bar technique has been used to investigate the dynamic behavior of hot-pressed BC under uniaxial and confined compressive strength tests. The results have shown a noticeable difference in the developed strength and macroscopic failure modes. It has been demonstrated that a relatively small confining pressure can effectively suppress the crack growth and thereby improve the mechanical performance of the material. However, a confined stress state does not change the mechanisms of fracture, and transgranular fracture has been reported in both cases. The SEM studies have also shown that the microstructural defects, such as large carbon inclusions, cause premature failure due to microcracking. A tensile character of these microcracks shows similarity to the wing crack model. Detailed TEM studies have revealed that the dislocations, deformation twins and grain boundaries do not contribute to the damage process even under higher confining stresses, which confirms that microstructural defects act as nucleation sites. Finally, a strain rate dependence for compressive fracture stress can be suggested if comparing the results obtained from the quasi-static and dynamic regimes. However, we note that the experimental setup used for confined compression tests under quasi-static loading is exploratory in nature, which, nonetheless, provides better understanding

of the behavior of BC under multiaxial stress state. To this end, these results can be employed as a validation for the models, guidance for processing of BC or improving application performance.

Acknowledgement

This work was sponsored by the Army Research Laboratory and was accomplished under Cooperative Agreement Number W911NF-12-2-0022. The views and conclusions contained in this document are those of the authors and should not be interpreted as representing the official policies, either expressed or implied, of the Army Research Laboratory or the U.S. Government. The U.S. Government is authorized to reproduce and distribute reprints for Government purposes notwithstanding any copyright notation herein.

Jeffrey J. Swab, Jerry LaSalvia and James W. McCauley (U.S. Army Research Laboratory) are acknowledged for many discussions on the dynamic behavior of boron carbide.

References

[1] D. L. Orphal, R. R. Franzen, A. C. Charters, T. L. Menna, A. J. Piekutowski, Penetration of confined boron carbide targets by tungsten long rods at impact velocities from 1.5 to 5.0 km/s, Int J Impact Eng 19 (1) (1997) 15–29. doi:10.1016/S0734-743X(96)00004-8.

[2] W. A. Gooch, M. S. Burkins, G. Hauver, P. Netherwood, R. Benck, Dynamic x-ray imaging of the penetration of boron carbide, J Phys IV France 10 (PR9) (2000) 583–588. doi:10.1051/jp4:2000997.

[3] M. Chen, J. W. McCauley, K. J. Hemker, Shock-induced localized amorphization in boron carbide, Science 299 (5612) (2003) 1563–1566. doi:10.1126/science.1080819.

[4] J. C. LaSalvia, R. B. Leavy, J. R. Houskamp, H. T. Miller, D. E. MacKenzie, J. Campbell, Ballistic impact damage observations in a hot-pressed boron carbide, in: J. Swab, D. Singh, J. Salem (Eds.), Advances in Ceramic Armor V, John Wiley & Sons, Inc., Hoboken, NJ, USA, 2010, pp. 45–55. doi:10.1002/9780470584330.ch5.

[5] S. G. Savio, K. Ramanjaneyulu, V. Madhu, T. B. Bhat, An experimental study on ballistic performance of boron carbide tiles, Int J Impact Eng 38 (7) (2011) 535–541. doi:10.1016/j.ijimpeng.2011.01.006.

[6] R. G. McQueen, S. P. Marsh, J. W. Taylor, J. N. Fritz, W. J. Carter, Chapter VII: The equation of state of solids from shock wave studies, in: R. Kinslow (Ed.), High-Velocity Impact Phenomena, Academic Press, New York, NY, USA, 1970, pp. 293–417. doi:10.1016/B978-0-12-408950-1.50012-4.

[7] W. H. Gust, E. B. Royce, Dynamic yield strengths of B4C, BeO, and Al2O3 ceramics, J Appl Phys 42 (1) (1971) 276–295. doi:10.1063/1.1659584.

[8] D. E. Grady, Shock-wave strength properties of boron carbide and silicon carbide, J Phys IV 04 (Colloque C8) (1994) C8–385–C8–391. doi:10.1051/jp4:1994859.

[9] T. J. Vogler, W. D. Reinhart, L. C. Chhabildas, Dynamic behavior of boron carbide, J Appl Phys 95 (8) (2004) 4173–4183. doi:10.1063/1.1686902.

[10] Y. Zhang, T. Mashimo, Y. Uemura, M. Uchino, M. Kodama, K. Shibata, K. Fukuoka, M. Kikuchi, T. Kobayashi, T. Sekine, Shock compression behaviors of boron carbide (B4C), J Appl Phys 100 (11) (2006) 113536–113700. doi:10.1063/1.2399334.

[11] V. Paris, N. Frage, M. P. Dariel, E. Zaretsky, The spall strength of silicon carbide and boron carbide ceramics processed by spark plasma sintering, Int J Impact Eng 37 (11) (2010) 1092–1099. doi:10.1016/j.ijimpeng.2010.06.008.

[12] K. M. Reddy, J. J. Guo, Y. Shinoda, T. Fujita, A. Hirata, J. Singh, J. W. McCauley, M. W. Chen, Enhanced mechanical properties of nanocrystalline boron carbide by nanoporosity and interface phases, Nat Commun 3 (2012) 1052. doi:10.1038/ncomms2047.

[13] R. D. Nixon, D. A. Koester, S. Chevacharoenkul, R. F. Davis, Steady-state creep of hot-pressed SiC whisker-reinforced silicon nitride, Compos Sci Technol 37 (13) (1990) 313–328. doi:10.1016/0266-3538(90)90107-G.

[14] K. T. Ramesh, G. Ravichandran, Dynamic behavior of a boron carbide aluminum cermet: experiments and observations, Mech Mater 10 (1) (1990) 19–29. doi:10.1016/0167-6636(90)90014-7.

[15] S. M. Wiederhorn, B. J. Hockey, D. C. Cranmer, R. Yeckley, Transient creep behaviour of hot isostatically pressed silicon nitride, J Mater Sci 28 (2) (1993) 445–453. doi:10.1007/BF00357822.

[16] W. R. Blumenthal, G. T. Gray III, T. N. Claytor, Response of aluminium-infiltrated boron carbide cermets to shock wave loading, J Mater Sci 29 (17) (1994) 4567–4576. doi:10.1007/BF00376280.

[17] W. Chen, G. Ravichandran, Dynamic compressive failure of a glass ceramic under lateral confinement, J Mech Phys Solids 45 (8) (1997) 1303–1328. doi:10.1016/S0022-5096(97)00006-9.

[18] W. Chen, G. Ravichandran, Failure mode transition in ceramics under dynamic multiaxial compression, Int J Fract 101 (1-2) (2000) 141–159. doi:10.1023/A:1007672422700.

[19] B. Paliwal, K. T. Ramesh, J. W. McCauley, M. Chen, Dynamic compressive failure of AlON under controlled planar confinement, J Am Ceram Soc 91 (11) (2008) 3619–3629. doi:10.1111/j.1551-2916.2008.02712.x.

[20] G. Hu, K. T. Ramesh, B. Cao, J. W. McCauley, The compressive failure of aluminum nitride considered as a model advanced ceramic, J Mech Phys Solids 59 (5) (2011) 1076–1093. doi:10.1016/j.jmps.2011.02.003.

[21] J. Lankford, C. E. Anderson Jr, G. R. Johnson, T. J. Holmquist, Dynamic compressive failure of ceramics under confinement, in: Proceedings of the 1991 Combat Vehicle Survivability Conference, Vol. 2, 1991, pp. 67–73.

[22] C. E. Anderson, B. L. Morris, The ballistic performance of confined Al2O3 ceramic tiles, Int J Impact Eng 12 (2) (1992) 167–187. doi:10.1016/0734-743X(92)90395-A.

[23] D. A. Shockey, A. H. Marchand, S. R. Skaggs, G. E. Cort, M. W. Burkett, R. Parker, Failure phenomenology of confined ceramic targets and impacting rods, Int J Impact Eng 9 (3) (1990) 263–275. doi:10.1016/0734-743X(90)90002-D.

[24] Y. Bao, S. Su, J. Yang, Q. Fan, Prestressed ceramics and improvement of impact resistance, Mater Lett 57 (2) (2002) 518–524. doi:10.1016/S0167-577X(02)00822-4.

[25] A. A. Griffith, The phenomena of rupture and flow in solids, Philos Trans R Soc Lond A 221 (1921) 163–198. doi:10.1098/rsta.1921.0006.

[26] G. R. Irwin, Analysis of stresses and strains near the end of a crack traversing a plate, J Appl Mech 24 (1957) 361–364.

[27] E. Hoek, Z. T. Bieniawski, Brittle fracture propagation in rock under compression, Int J Fract 1 (3) (1965) 137–155. doi:10.1007/BF00186851.

[28] A. Hillerborg, M. Modeer, P. E. Petersson, Analysis of crack formation and crack growth in concrete by means of fracture mechanics and finite elements, Cem Concr Res 6 (6) (1976) 773–781. doi:10.1016/0008-8846(76)90007-7.

[29] H. Wang, K. T. Ramesh, Dynamic strength and fragmentation of hot-pressed silicon carbide under uniaxial compression, Acta Mater 52 (2) (2004) 355–367. doi:10.1016/j.actamat.2003.09.036.

[30] J. D. Hogan, L. Farbaniec, M. Shaeffer, K. T. Ramesh, The effects of microstructure and confinement on the compressive fragmentation of an advanced ceramic, J Am Ceram Soc 98 (3) (2015) 902–912. doi:10.1111/jace.13353.

[31] L. Farbaniec, J. D. Hogan, K. T. Ramesh, Micromechanisms associated with the dynamic compressive failure of hot-pressed boron carbide, Scripta Mater 106 (2015) 52–56. doi:10.1016/j.scriptamat.2015.05.004.

[32] J. D. Hogan, L. Farbaniec, T. Sano, M. Shaeffer, K. T. Ramesh, The effects of defects on the uniaxial compressive strength and failure of an advanced ceramic, Acta Mater 102 (2016) 263–272. doi:10.1016/j.actamat.2015.09.028.

[33] L. Farbaniec, J. D. Hogan, J. W. McCauley, K. T. Ramesh, Anisotropy of mechanical properties in a hot-pressed boron carbide, Int J Appl Ceram Technol (Advance online publication) (2016) 1–9. doi:10.1111/ijac.12585.

[34] T. Jiao, Y. Li, K. T. Ramesh, A. A. Wereszczat, High rate response and dynamic failure of structural ceramics, Int J Appl Ceram Technol 1 (3) (2004) 243–253. doi:10.1111/j.1744-7402.2004.tb00176.x.

[35] D. Ghosh, G. Subhash, J. Q. Zheng, V. Halls, Influence of stress state and strain rate on structural amorphization in boron carbide, J Appl Phys 111 (6) (2012) 063523. doi:10.1063/1.3696971.

[36] G. Hu, C. Q. Chen, K. T. Ramesh, J. W. McCauley, Dynamic multiaxial response of a hot-pressed aluminum nitride, Scripta Mater 66 (8) (2012) 527–530. doi:10.1016/j.scriptamat.2011.12.037.

[37] J. Lankford, Mechanisms responsible for strain-rate-dependent compressive strength in ceramic materials, J Am Ceram Soc 64 (2) (1981) C–33–C–34. doi:10.1111/j.1151-2916.1981.tb09570.x.

[38] J. Lankford, High strain rate compression and plastic flow of ceramics, J Mater Sci Lett 15 (9) (1996) 745–750. doi:10.1007/BF00274593.

[39] H. Horii, S. Nemat-Nasser, Brittle failure in compression: splitting, faulting and brittle-ductile transition, Phil Trans R Soc Lond A 319 (1549) (1986) 337–374. doi:10.1098/rsta.1986.0101.

[40] C. Huang, G. Subhash, Influence of lateral confinement on dynamic damage evolution during uniaxial compressive response of brittle solids, J Mech Phys Solids 51 (6) (2003) 1089–1105. doi:10.1016/S0022-5096(03)00002-4.

[41] M. F. Ashby, S. D. Hallam, The failure of brittle solids containing small cracks under compressive stress states, Acta Metall 34 (3) (1986) 497–510. doi:10.1016/0001-6160(86)90086-6.

[42] M. F. Ashby, C. G. Sammis, The damage mechanics of brittle solids in compression, Pure Appl Geophys 133 (3) (1990) 489–521. doi:10.1007/BF00878002.

[43] M. Janssen, J. Zuidema, R. Wanhill, Fracture Mechanics, Second Edition: Fundamentals and Applications, Spon Press, Taylor & Francis Group: London and New York, 2004.

[44] J. Rey, P. Kapsa, G. Male, Dry friction and wear of chemically vapour deposited boron carbide coatings, Surf Coat Technol 36 (1) (1988) 375–386. doi:10.1016/0257-8972(88)90167-3.

[45] J. C. LaSalvia, M. J. Normandia, H. T. Miller, D. E. Mackenzie, Sphere Impact Induced Damage in Ceramics: I. Armor-Grade SiC and TiB2, in: J. J. Swab (Ed.), Advances in Ceramic Armor: A Collection of Papers Presented at the 29th International Conference on Advanced Ceramics and Composites, January 23-28, 2005, Cocoa Beach, Florida, Ceramic Engineering and Science Proceedings, Volume 26, Number 7, John Wiley and Sons, Inc., Hoboken, NJ, USA, 2008, pp. 170–181. doi:10.1002/9780470291276.ch20.

[46] J. C. LaSalvia, M. J. Normandia, H. T. Miller, D. E. MacKenzie, Sphere Impact Induced Damage in Ceramics: II. Armor-Grade B4C and WC, in: J. J. Swab (Ed.), Advances in Ceramic Armor: A Collection of Papers Presented at the 29th International Conference on Advanced Ceramics and Composites, January 23-28, 2005, Cocoa Beach, Florida, Ceramic Engineering and Science Proceedings, Volume 26, Number 7, John Wiley and Sons, Inc., Hoboken, NJ, USA, 2008, pp. 183–192. doi:10.1002/9780470291276.ch21.

List of Figures

static compression, where exposed are: (a) the free surface of the sample; (b) the surface that was in contact with the WC disk, and which experienced the major compressive load (the direction of the largest compressive principal loading is normal to the image plane). The main compression axis and confinement axis are indicated by the blue and green arrows, respectively.

Figure 9. TEM micrographs showing characteristic fragments of the specimen that was subjected to confined dynamic compression: (a) typical damage-free fragment; (b) cleavage steps as a consequence of the crack propagation through neighboring grains with highly twisted boundaries; (c) internal grain structure of the fragment that was polished to electron transparency; (d) grain structure of the intact material with the indicated carbon inclusion (labelled as 'C').

Figure 10. Failure processes in uniaxial and confined compression tests.

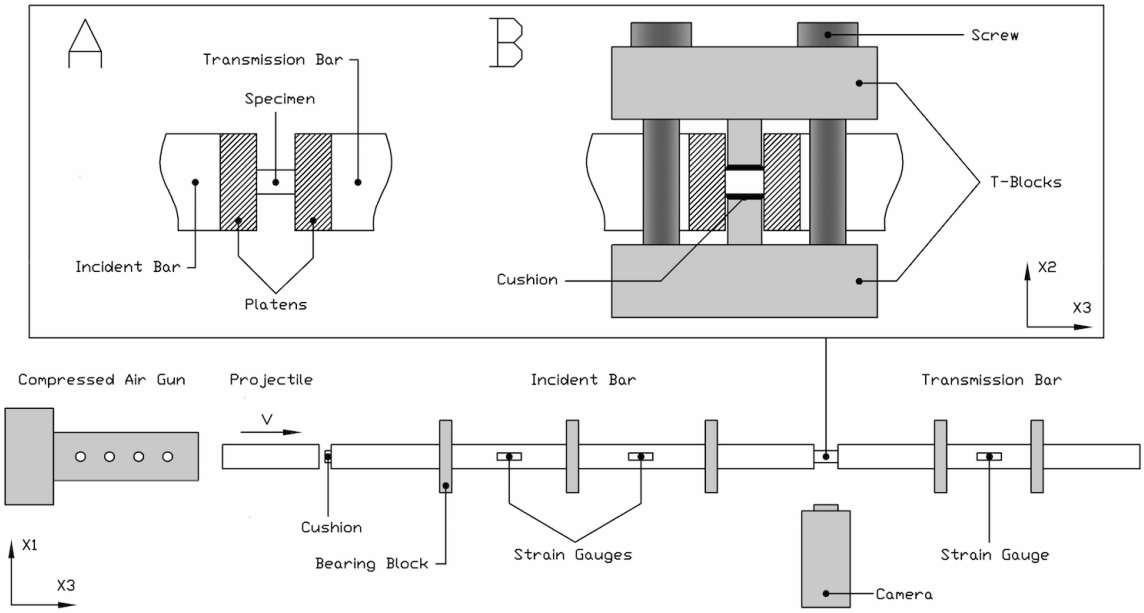
A
Transmission Bar
Specimen
Incident Bar
Platens
B
Screw
T-Blocks
Cushion
X2
X3
Compressed Air Gun
Projectile
Incident Bar
Transmission Bar
V
Cushion
Bearing Block
Strain Gauges
Strain Gauge
Camera
X1
X3

Figure 1

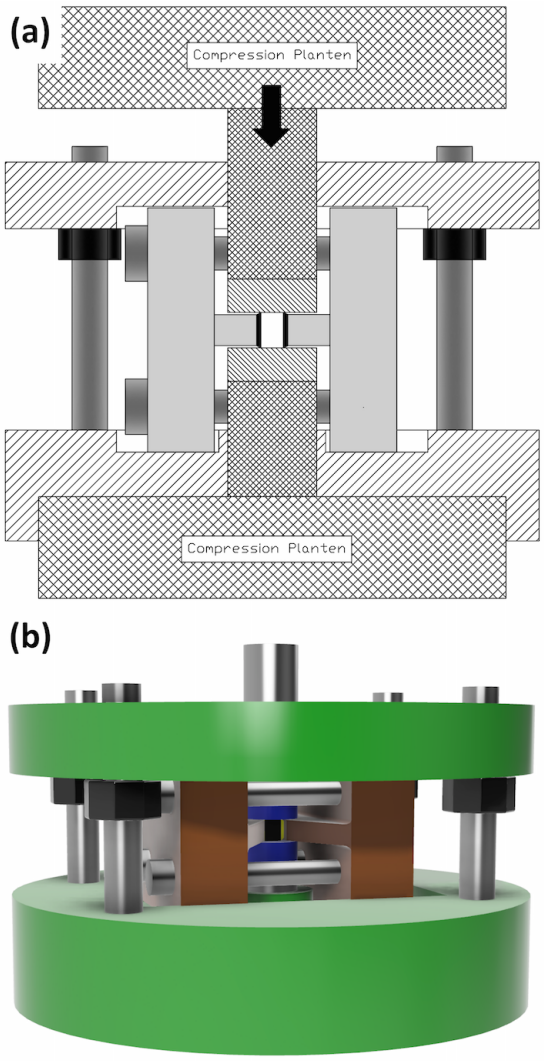

Figure 2

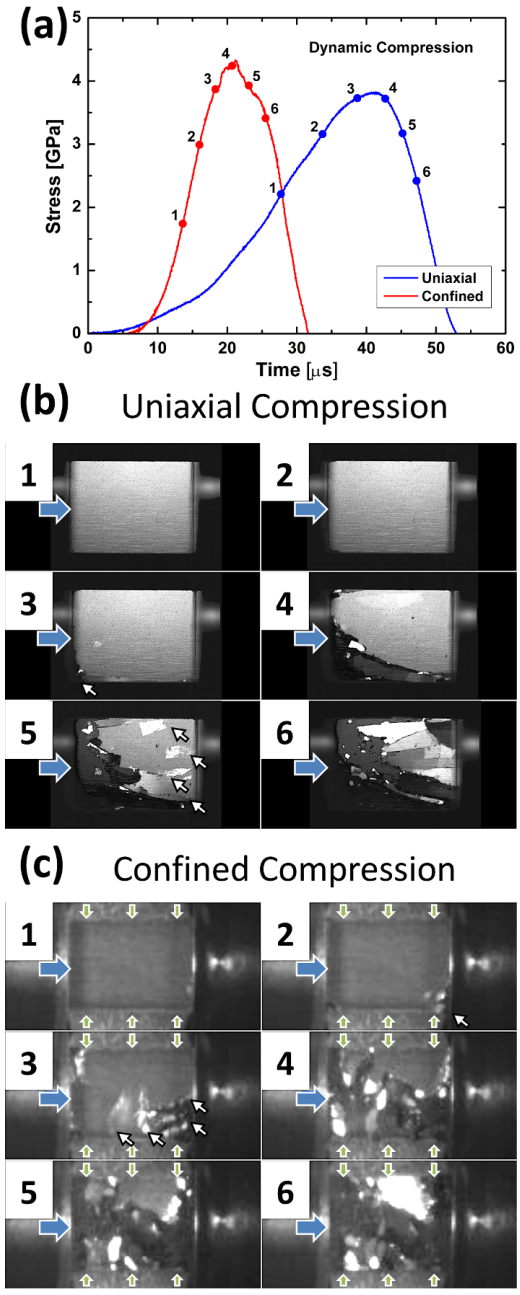
(a)
Dynamic Compression
Stress [GPa]
Time [μs]
Uniaxial
Confined
(b) Uniaxial Compression
(c) Confined Compression

Figure 3

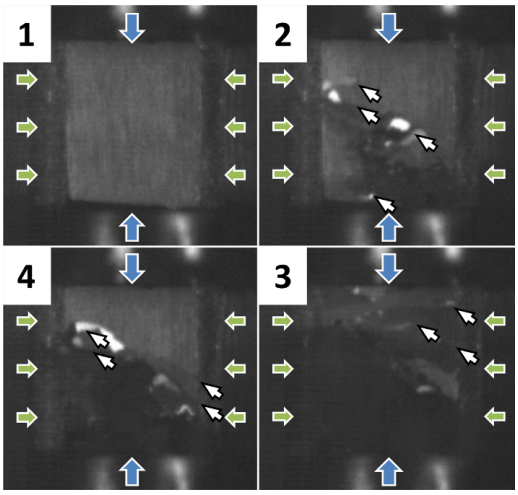

Figure 4

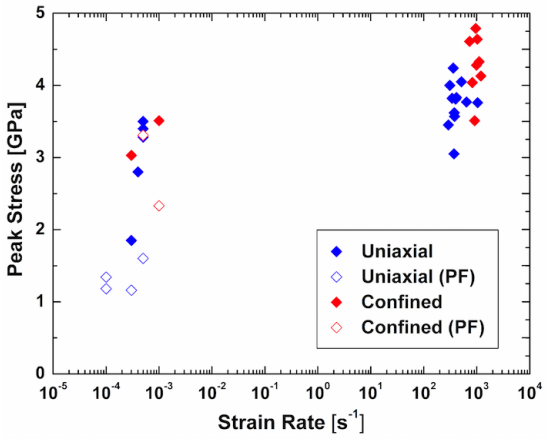
Peak Stress [GPa]
Strain Rate [s^{-1}]
Uniaxial
Uniaxial (PF)
Confined
Confined (PF)

Figure 5

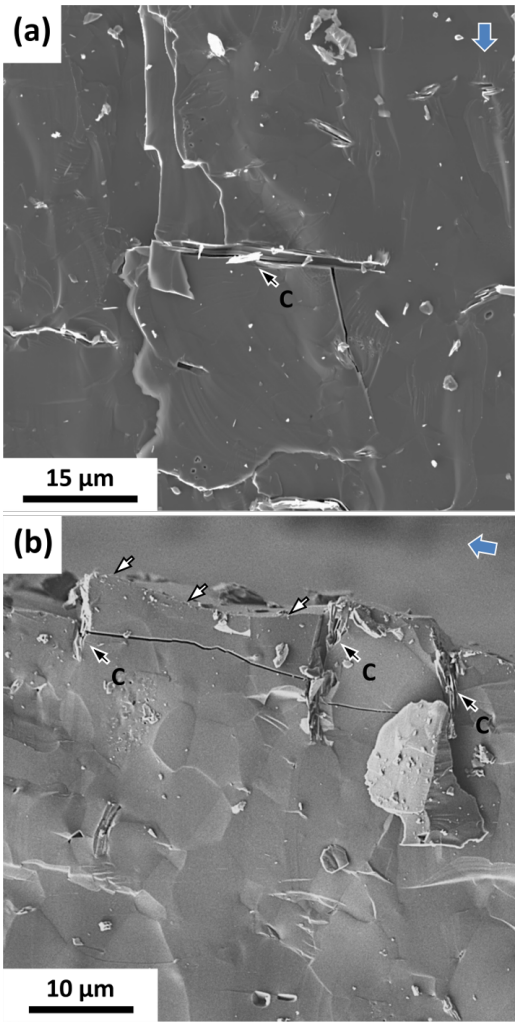

Figure 6

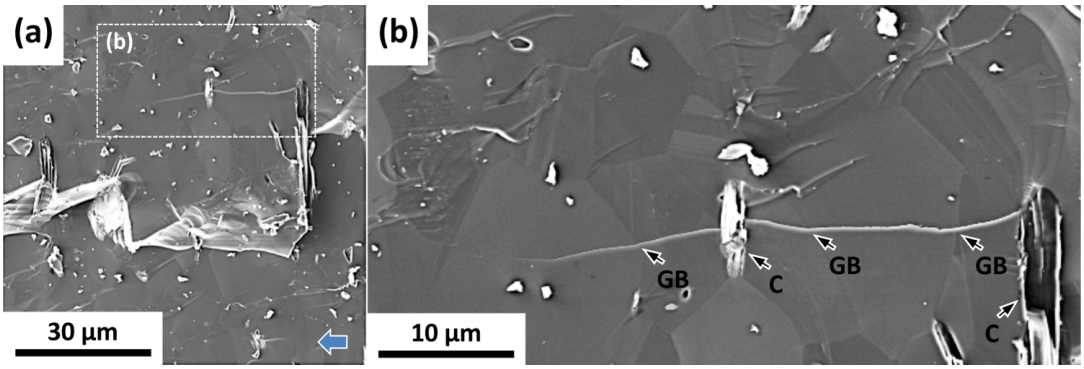

Figure 7

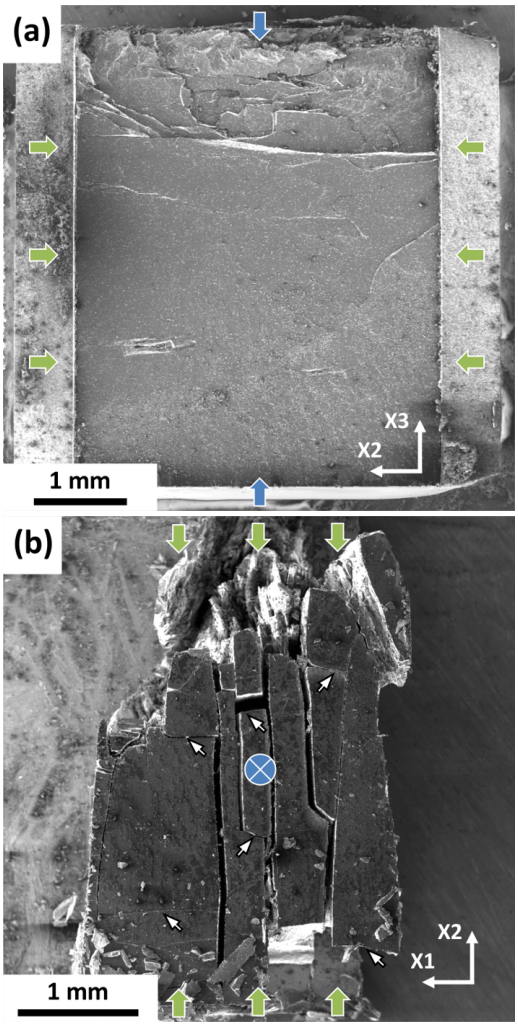

630

Figure 8

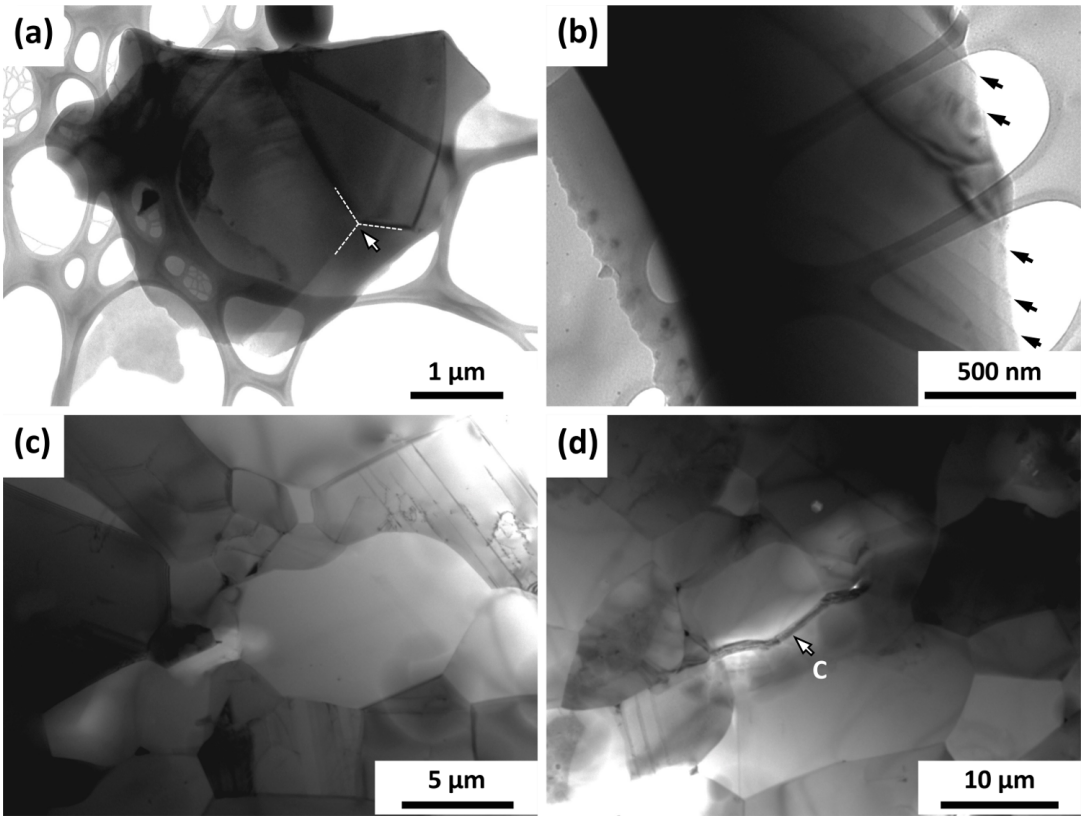

Figure 9

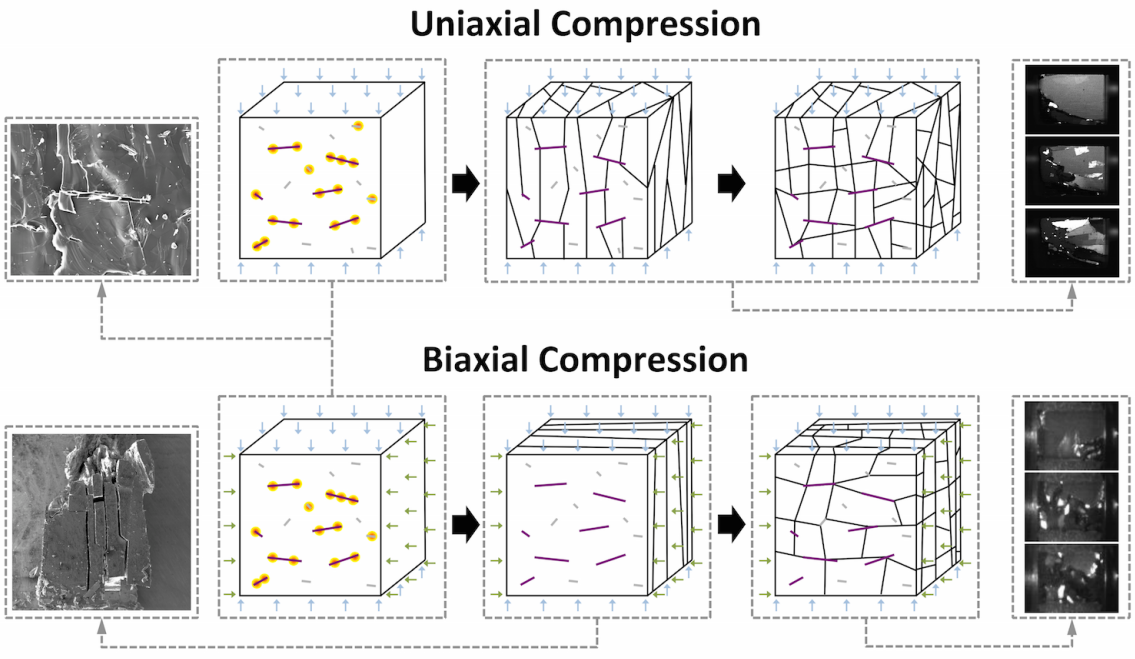

Figure 10